
Interpretable Water Level Forecaster with Spatiotemporal Causal Attention Mechanisms

Sungchul Hong, Yunjin Choi and Jong-June Jeon*

Department of Statistics

University of Seoul

{shong, ycstat, jj.jeon}@uos.ac.kr

Abstract

Forecasting the water level of the Han River is essential to control traffic and avoid natural disasters. The stream flow of the Han River is affected by various and intricately connected factors. Thus, a simple forecasting machine frequently fails to capture its serial pattern. On the other hand, a complex predictive model loses the interpretability of the model output. This work proposes a neural network model with a novel transformer exploiting a causal relationship based on prior knowledge. The transformer consists of spatiotemporal attention weight that describes the spatial and temporal causation with multilayer networks with masking. Our model has two distinguished advantages against the existing spatiotemporal forecasting models. First, the model allows the heterogeneous predictors for each site such that a flexible regression is applicable to the causal network. Next, the model is adapted to partially identified causal structures. As a result, we have relaxed the constraints of the applicable causal network through our model. In real data analysis, we use the Han River dataset from 2016 to 2021, compare the proposed model with deep learning models, and confirm that our model provides an interpretable and consistent model with prior knowledge, such as a seasonality arising from the tidal force. Furthermore, in prediction performance, our model is better than or competitive with the state-of-the-art models.

Keywords: Water level forecasting, Spatiotemporal dependence, Transformer, Interpretable AI

*Corresponding author.

1 Introduction

With dramatic advances in computation and large scaled data storage, predictive models trained by a neural network are widely used in various industries and sectors such as finance, health care, and logistic management(Chatigny et al., 2021; Sezer et al., 2020; Avati et al., 2017; Kaneko & Yada, 2016). The predictive model automatically and periodically updates the model parameters by monitoring its performance, and it rapidly replaces simple and monotonous work conducted by humans. The widespread use of neural network models owes to their predictive performance and flexibility for various task-oriented purposes(Begoli et al., 2019; Benidis et al., 2020; Carion et al., 2020; Shen et al., 2018).

However, when the neural network model fails to provide a sound prediction output, which is not expected in the model training phase, its diagnosis and modification are generally challenging. Because compositions of multiple nonlinear functions construct the neural network model, the relation between input and output is not directly accounted for by the model parameters. The lack of accountability for the model output undermines the model's trustworthiness and discourages using the neural network model.

In developing a water level forecasting model, the need for the model interpretability has been raised in the same context(Aguilera et al., 2019; Ding et al., 2020; Castangia et al., 2023). The model interpretability is required, mainly when the forecasting model provides a differing outcome from the expert's opinion or physics law. Even when the neural network model outperforms the experts, it is not easy to accept the result produced by the machine without a confirmative analysis. In the expert domain, the predictive model necessarily follows known physics laws, and typically there

are two types of issues for water level forecasting, spatial dependency and temporal dependency (Wu et al., 2020; Noor et al., 2022).

The spatial dependency is primarily related to the network structure consisting of multiple downstream. Geomorphologic factors, including the width of rivers, the structure of linked streams, and the height around the basin, affect the water levels observed on multiple sites. The station gauging water level is usually regarded as a node, and the river stream is modeled as an edge on the network. The temporal dependency is closely related to the physical attributes of water flow explained by fluid dynamics. In a closed system, the water flow upstream directly determines that of downstream, and estimating water levels is of primary interest as a functional form on time.

In the real world, the two types of dependencies are entangled. Conventional machine learning models employ the two-step approach of filtering temporal dependence and constructing a spatial dependence to incorporate the dependencies. The temporal filter, such as autoregressive model, wavelet transformation, and empirical mode decomposition, extracts a temporal feature in the systematic pre-processing phase (Yadav & Eliza, 2017; Wu et al., 2021). The filtered temporal features of multiple sites are spatially aggregated in the nonlinear models such as the support vector machine, the neural network model, and the neuro-fuzzy system (Ruslan et al., 2014; Yadav & Eliza, 2017). Thus, the interpretability of the two types of dependencies disappears in the forecasting model due to the use of the complex model.

We tackle the challenging problem of developing a neural network model in which the spatial and temporal dependencies can be explained simultaneously. Our model has two attention weights accounting for correlations between spatial and temporal features. Each attention weight is masked to enforce the features following our prior knowledge, such as temporal causality and spatial physics law. The trained model explains a causal structure across spatial and temporal features and forecasts results by restricting the model space. Besides, spatial features are summarized by a site-specific embedding layer, and thus the proposed model employs a multilayer network that allows spatially heterogeneous predictors and partially identified causal structures. This flexibility is a remarkable advance in a model structure for a spatiotemporal forecaster compared to the existing models.

Section 2 investigates the related work of presenting neural network models for spatiotemporal data analysis. Section 3 introduces river network data of interest in this paper and model assumptions dominated

by physics law. Section 4 explains the proposed model focusing on new spatiotemporal attention. Section 5 shows the numerical result from river network data analysis, which provides explainable quantities for understanding a complex network. Concluding remarks follow in Section 6.

We briefly introduce notations frequently used throughout our paper. For a vector $\mathbf{x} \in \mathbb{R}$, $\mathbf{x}_{i:j}$ denotes the sliced vector from the i^{th} element to the j^{th} element of \mathbf{x} . For a matrix $M \in \mathbb{R}^{m \times n}$, $(M)_{ij}$ denotes the element of the i^{th} row and the j^{th} column. $M_{i_1:i_2, j_1:j_2}$ denotes the submatrix sliced from i_1^{th} row to i_2^{th} row and from j_1^{th} column to j_2^{th} column. When the row or the column index is omitted, the slicing is not applied to the rows or the columns.

2 Related Work

This section introduces probabilistic forecasting, interpretable AI, spatiotemporal modeling, and their related works.

Probabilistic forecasting. Probabilistic forecaster provides not point estimates but more informative quantities about target variables, such as a conditional distribution or multiple quantiles for decision-making. The state-of-the-art models exploit as many features as possible, including historical, categorical, and even future information, such as the date and weekly predicted weather, to forecast the target variable accurately. Many deep learning-based probabilistic forecasters, such as DeepAR (Salinas et al., 2020), MQ-RNN (Wen et al., 2017), and TFT (Lim et al., 2021), have been proposed and are being widely used in various domains due to their powerful performances.

Interpretable AI. Interpretable AI has accelerated the development of reliable models in water resource management (Ding et al., 2020; Castangia et al., 2023). Many applications have been conducted based on a TFT, which has improved interpretability and notable predictive performances (Civitaresse et al., 2021; Castangia et al., 2023). The TFT is a transformer-based model that quantifies the importance of variables with a variable selection network and attention mechanism, thereby enhancing interpretability. However, a complex data structure such as spatial dependencies or heterogeneous data incurs a failure to assess the importance of variables.

Spatiotemporal modeling. In hydrological time series forecasting, spatial modeling is also crucial as temporal dynamics modeling so that the two regimes are simultaneously considered with the framework of the spatiotemporal stochastic structure. The deep learning-based models are spotlighted due to their

straightforwardness of spatiotemporal modeling. There are two mainstream types to construct the deep learning model as follows. The first approach combines a canonical forecasting model with a graph neural network (GNN). The GNN-based models learn spatial dependencies using graph convolution network (GCN) and temporal patterns using recurrent neural network (RNN), temporal attention, or temporal convolution network (TCN) (Deng et al., 2022). However, these models have limitations because the model structure is not flexible enough to include heterogeneous types of spatial-temporal predictors across sites. The second approach is a restriction of model architecture to compel the spatiotemporal dependencies (Ding et al., 2020; Liu et al., 2022). These models are designed for specific domains or spatial structures, so their architectures need to be altered for new spatial structures.

Unlike the aforementioned methods, we propose a general model that simultaneously works with spatiotemporal dependencies and heterogeneous data. Our model proposes a simple architecture instead of the GNN to model spatiotemporal structure and surpasses TFT in terms of interpretability.

3 Dataset and Preliminary

3.1 Dataset

The Jamsu Bridge connects the central business districts on the Han River’s north and south sides. Due to the Jamsu Bridge’s susceptibility to flooding, it is imperative to anticipate potential flooding risks and regulate traffic accordingly. The data* to be used for predicting the water level of the Jamsu Bridge are collected from six observatories on the Han River network and three other meteorological observatories. The observatories on the river network are Paldang Dam (D), Cheongdam Bridge (B_1), Jamsu Bridge (B_2), Hangang Bridge (B_3), Haengju Bridge (B_4), and Ganghwa bridge (B_5). The time series data collected in Paldang Dam are water level (WL), inflow (IF), outflow (OF), storage (STR), and joint usage storage (JUS). The water level and flow data are collected in four other observatories except for the Jamsu Bridge. In the Jamsu Bridge, only water level data are collected.

We use additional variables, precipitations of three sites (P_1 , P_2 , and P_3) around the Han River, and temporal variables (month, day, and hour). Except for the temporal variables, all other variables are summarized hourly. The dataset encompasses the entire period from

2016 to 2021. Our study’s spatial coverage is displayed in Figure 1, while the summary statistics for the variables employed are delineated in the Appendix.

Part of observed multivariate data essentially follows a law of spatiotemporal causality. But the causality is partially identified due to a lack of information. For example, both the outflow of a dam and precipitation increases the water levels of the Jamsu bridge. As a non-trivial example, the water level of the Ganghwa Bridge, located downstream, can affect those of other bridges. Because of the tidal nature of the Han River, the water level at the Ganghwa Bridge serves as a crucial predictor for inferring the water level at the Jamsu Bridge (Park & Baek, 2017; Jung et al., 2018). Meanwhile, only correlation can be identified for observed variables such as precipitation data. The challenge is to model the temporal dependence, spatial causality, and variable correlation simultaneously when the spatiotemporal causal structure is only partially identified. To address this issue, we propose a multilayer network for spatiotemporal modeling.

3.2 Multilayer Network for Spatiotemporal Modeling

A multilayer network is a useful tool for modeling a pattern across variables with a hierarchical structure (Kivelä et al., 2013), such as biomedicine (Hammoud & Kramer, 2020) and community detection (Huang et al., 2020). Spatial causality is modeled on a single layer as a directed graph for a fixed time. A temporal dependency among the causal graphs is represented by a directed edge. Choi et al. (2022) captured spatiotemporal patterns of the bike-sharing system by stacking layers along the time axis in the multilayer network.

Motivated by the precedent studies, we utilize the multilayer network for representation learning of spatiotemporal variables. First, basing ourselves on results by prior knowledge and analyses of the Han River (Shin & Yoon, 2005; Park & Baek, 2017), we group the sites in the research area into four clusters: $C_1 = \{P_1, P_2, P_3\}$, $C_2 = \{B_5\}$, $C_3 = \{D\}$ and $C_4 = \{B_1, B_2, B_3, B_4\}$. Define a node $v_{s,t}$ representing all observations available in the cluster C_s , $s \in \mathcal{S} = \{1, 2, 3, 4\}$ and at the time $t \in \mathcal{T} = \{1, \dots, T\}$. The causal structures between $v_{s,t}$ s are modeled by the directed edges in a causal graph \mathcal{G} . Let \mathcal{G} be a multilayer network, a tuple defined by a set of nodes \mathcal{V} , a set of edges \mathcal{E} , and a set of layers.

$$\mathcal{G} = (\mathcal{V}, \mathcal{E}, \mathcal{T}), \mathcal{V} = \bigcup_{t \in \mathcal{T}} V_t,$$

where $V_t = \{v_{1,t}, \dots, v_{4,t}\}$. Assumption 1 and 2 defines

*dacon.io

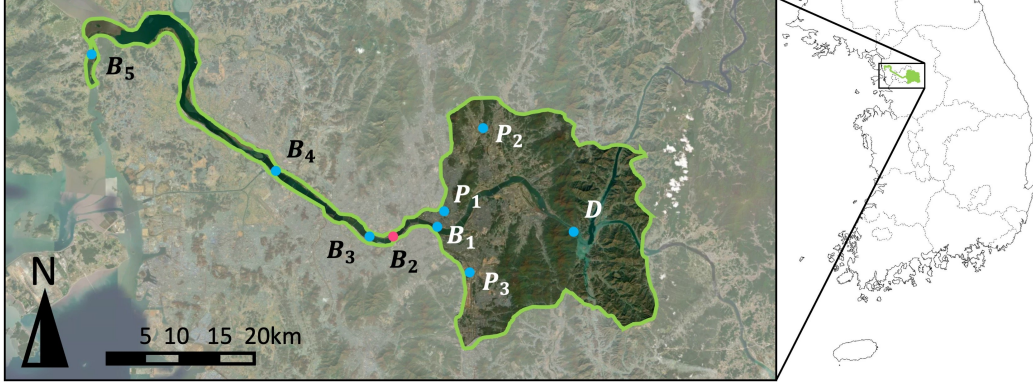


Figure 1: Research area, the Han River in Seoul, South Korea. The blue points are spatial sites, and the red denotes our target site, the Jamsil bridge B_2 . The river from the east flows into the sea on the west.

the causal structure of our model.

Assumption 1. (Temporal Causality) For $s, s' \in \mathcal{S}$ and $t, t' \in \mathcal{T}$, the multilayer network $\mathcal{G} = (\mathcal{V}, \mathcal{E}, \mathcal{T})$ satisfies the following conditions:

1. Suppose that $t \leq t'$, then $(v_{s,t'}, v_{s,t}) \notin \mathcal{E}$.
2. For $s \neq s'$ and $(v_{s,t}, v_{s',t}) \in \mathcal{E}$ if and only if $(v_{s,t'}, v_{s',t'}) \in \mathcal{E}$. In addition, $(v_{s,t}, v_{s',t}) \notin \mathcal{E}$ if and only if $(v_{s,t'}, v_{s',t'}) \notin \mathcal{E}$.

Assumption 1.1 implies the irreversibility, and Assumption 1.2 means the homogeneous spatial causality along time. The spatiotemporal causality is established on the multilayer network by Assumption 2.

Assumption 2 (Spatial Causality). $(v_{s,1}, v_{s',1}) \in \mathcal{E}$, if $(s, s') \in \{(1, 3), (1, 4), (2, 4), (4, 3)\}$. Otherwise, $(v_{s,1}, v_{s',1}) \notin \mathcal{E}$.

Assumption 2 specifically defines spatial causality based on our prior knowledge. The directed edges need to be estimated for a case. Still, our study assumes they are known because we focus on constructing an embedded feature space for spatiotemporal data. If the time indices are omitted, the causalities are summarized as

$$v_1 \rightarrow v_3, v_1 \rightarrow v_4, v_2 \rightarrow v_4, v_3 \rightarrow v_4, \quad (1)$$

where the arrow denotes the causation. For example, $v_1 \rightarrow v_3$ means that v_1 is *cause* or *parent* of v_3 and denote the causal relation by $v_1 \in \text{Pa}(v_3)$. We follow the notation of the causal relation between v_i and v_j by using $v_i \in \text{Pa}(v_j)$.

The node v_1 represents precipitation values of three sites (P_1, P_2, P_3), and we regard it as a globally influential variable. v_2 is the node corresponding to the

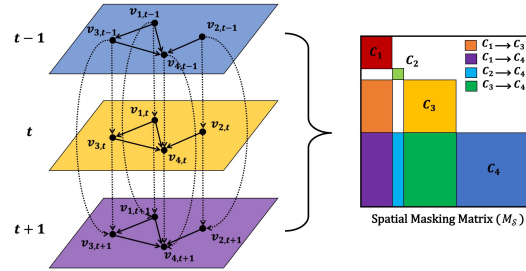


Figure 2: The multilayer network (left) for the Han River from time point $t-1$ to $t+1$. Under the proposed multilayer network \mathcal{G} , all layers have causal structure (1) identically, and the spatial masking matrix (right) is designed as M_S . The elements of squares on the diagonal enable us to model dependencies of variables in each site, and the elements of rectangular on the non-diagonal consider the causal relationship between sites. The details of M_S are discussed in Section 4.1.

Ganghwa Bridge, B_5 . The Han River is a tidal river whose flow and level are affected by tides, and the Ganghwa Bridge is located in the downstream area of the river (Park & Baek, 2017). Jung et al. (2018) thought highly of the predicted tide level of B_5 as the most important covariate. v_3 is related to the Paldang dam (D) located in the river's upper stream and affects the Han River's water level directly. That is, it is reasonable that $\text{Pa}(v_4) = \{v_1, v_2, v_3\}$. The spatial causality considered in our study is described in Table 1. The multilayer network \mathcal{G} for the Han River dataset based on the structure (1) is displayed in Figure 2.

Table 1: The descriptions of physical meaning of causations (1).

Causation	Description
$v_1 \rightarrow v_3$	The precipitations affect the variables of the dam D .
$v_1 \rightarrow v_4$	The precipitations affect the water levels and flow at the bridges in C_4 .
$v_2 \rightarrow v_4$	The variables at the bridge B_5 affect the water levels and flows at the bridges in C_4 .
$v_3 \rightarrow v_4$	The variables of the dam D affect the water levels and flows at the bridges in C_4 .

3.3 Attention Mechanism

Attention is a specific mapping from a sequence to a sequence. Let V be a $t \times d$ matrix whose each row vector denotes an element in a sequence with length t then the attention returns a $t \times d'$ matrix V' for the input V . In our study, the attention function reduces features of spatiotemporal data on the multilayer network. The attention employs two matrices $Q \in \mathbb{R}^{t \times d}$ and $K \in \mathbb{R}^{t \times d}$ associated with the target and input sequence. The attention for V is defined by

$$\text{Attention}(Q, K, V) = \text{softmax} \left(QK^\top / \sqrt{d} \right) V, \quad (2)$$

where softmax is a row-wise softmax function. In particular,

$$A = \text{softmax} \left(QK^\top / \sqrt{d} \right)$$

is called the attention weight.

We can identify or control a characteristic of trained features from the attention weight. Let a_{ij} be $(A)_{ij}$ and v_i and v'_i be the i th row vectors of V and $\text{Attention}(Q, K, V)$, respectively. Then it is easily shown that $v'_i = \sum_{j=1}^t a_{ij} v_j$. If we let M be $t \times t$ matrix and assign the minus infinity to $(M)_{ij}$, then $a_{ij} = 0$, which excludes v_j in consisting of a feature v'_i . Therefore, by assigning the minus infinity on the element of M , we can cut off the directed edge in the row vectors of V and construct a causal relationship for V .

When Q , K , and V represent the same sequence, (2) is called self-attention. In self-attention, the three matrices have different representations in the same sequence. Let $X \in \mathbb{R}^{t \times d'}$ be an input sequence, then the features in the self-attention are given by $Q = XW_Q$, $K = XW_K$ and $V = XW_V$, where $W \in \mathbb{R}^{d' \times d}$. The self-attention is written by a map from $\mathbb{R}^{t \times d'}$ to $\mathbb{R}^{t \times d}$ with three weight parameter matrices. Denote the self-attention of an input X with a masking matrix M by

$$\begin{aligned} & \mathcal{Z}(X; \mathbf{W}, M) \\ &= \text{softmax} \left(XW_Q(XW_K)^\top / \sqrt{d} \odot M \right) XW_V, \end{aligned} \quad (3)$$

where $\mathbf{W} = (W_Q, W_K, W_V)$ and \odot is the elementwise product operator. In this paper, \mathbf{W} is a tuple of trainable weight matrices, and M is a known masking matrix.

4 Proposed Model

This section proposes the InstaTran (interpretable spatiotemporal attention transformer), an interpretable transformer embedding the spatiotemporal dependencies with \mathcal{G} . The overall architecture of the proposed model is shown in Figure 3. We spell out the notations used throughout this section. Note that all vectors are row vectors (not column vectors).

4.1 Outline of Model Architecture

Let $\mathbf{x}_t^{(s)} \in \mathbb{R}^{p_s}$ for $s \in \mathcal{S}, t \in \mathcal{T}$ be a vector of explanatory variables to $v_{s,t}$ and denote a collection of the variables across all sites at time t by $\mathbf{x}_t = (\mathbf{x}_t^{(1)}, \dots, \mathbf{x}_t^{(4)}) \in \mathbb{R}^p$ with $p = \sum_{s \in \mathcal{S}} p_s$. Note that each $\mathbf{x}_t^{(s)}$ for s is allowed to be a heterogeneous variable defined on \mathbb{R}^{p_s} . Each component in \mathbf{x}_t is denoted by $x_{i,t}, i = 1, \dots, p$. We define a consecutive partition of $\{1, \dots, p\}$ by $\mathcal{I} = \{I_1, \dots, I_4\}$ where I_s represents the indices of the components of $\mathbf{x}_t^{(s)}$ within \mathbf{x}_t . By definition, the cardinality of I_s is equal to p_s . Denote month, day, and hour at time t by $u_{1,t}, u_{2,t}$ and $u_{3,t}$ and let $\mathbf{u}_t = (u_{1,t}, u_{2,t}, u_{3,t}) \in \mathbb{R}^3$. Note that \mathbf{u}_t is known for all t .

Our model aims to estimate a temporal series with length τ for multiple quantiles. Denote the q -quantile of estimated water level at a time t by $\hat{y}_{t,q}$ for $q \in \mathcal{Q}$. The model takes two series $\mathcal{X}_{t,B} = (\mathbf{x}_{t'} : t-B < t' \leq t)$ and $\mathcal{U}_{t,B}^\tau = (\mathbf{u}_{t'} : t-B < t' \leq t+\tau)$ as input data; it returns an estimated series $\hat{\mathbf{y}}_{t,q}^\tau = (\hat{y}_{t',q} : t < t' \leq t+\tau)$ for $q \in \mathcal{Q}$. The inputs $\mathcal{X}_{t,B}$ and $\mathcal{U}_{t,B}^\tau$ are embedded by the neural network with attention in (3). The spatiotemporal causal structure of variables in $\mathcal{X}_{t,B}$ is modeled by two types of masking matrices, the spatial masking matrix $M_S \in \mathbb{R}^{p \times p}$ and the temporal decoder mask M_T . M_S is determined by a known spatial causality presented in Table 1, and its element $m_{ij} := (M_S)_{ij}$ is given by

$$m_{ij} = \begin{cases} 1, & \text{if } i \in I_s, j \in I_{s'} \text{ and } v_{s'} \in \text{Pa}(v_s) \cap \{v_s\} \\ -\infty, & \text{otherwise.} \end{cases}$$

M_T equals the attention mask used in a typical language transformer (Vaswani et al., 2017).

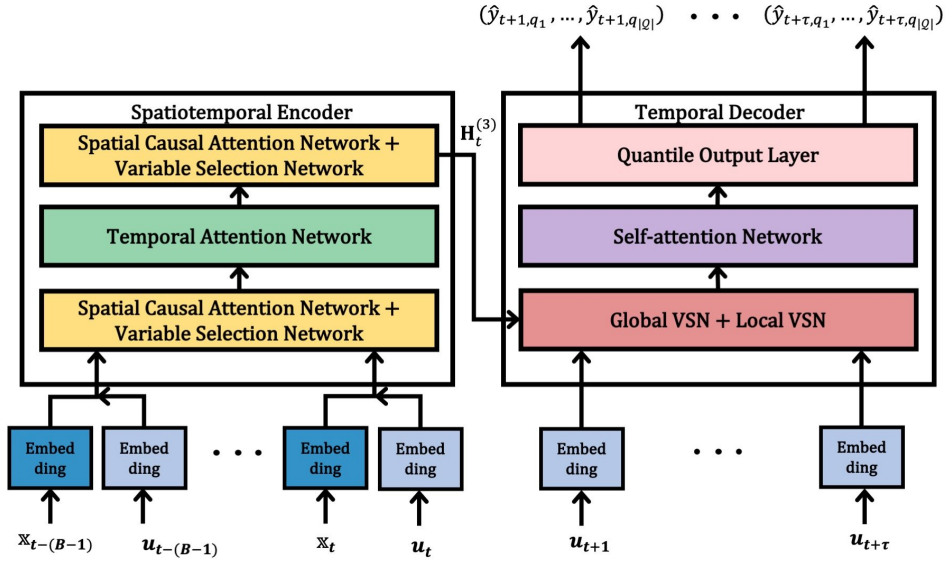
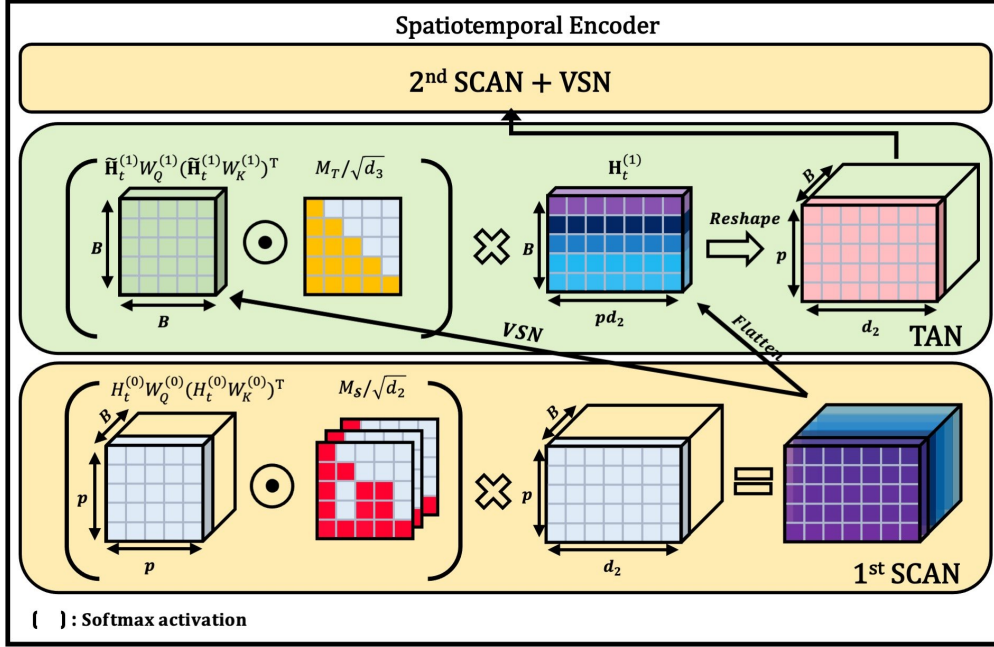


Figure 3: Architecture of proposed model (bottom) and details on SCAN and TAN (top).

Our forecasting model is obtained by F predicting

$$\hat{\mathbf{y}}_{t,Q}^\tau = F(\mathcal{X}_{t,B}, \mathcal{U}_{t,B}^\tau, M_S, M_T),$$

where $\hat{\mathbf{y}}_{t,Q}^\tau$ represents a tuple $(\hat{y}_{t,q}^\tau, q \in Q)$. The InstaTran consists of a spatiotemporal encoder and a temporal decoder. The spatiotemporal encoder learns a representation of variables included in the model, and the

temporal decoder produces multiple quantiles of future water levels.

4.2 Spatially Causal Attention Network

The spatially causal attention network (SCAN) is a self-attention to embed a collection of observed vari-

ables according to the known spatially causal relations in Table 1. The embedded feature presents aggregated information of all sites for a fixed time, and its spatial causation is reflected by the spatial masking matrix M_S .

All variables are initially embedded on \mathbb{R}^{d_1} . Let $g_i : \mathbb{R} \mapsto \mathbb{R}^{d_1}$ be a embedding function of $x_{i,t}$ in \mathbf{x}_t and $\tilde{g}_j : \mathbb{R} \mapsto \mathbb{R}^{d_1}$ be a embedding function of $u_{j,t}$ in \mathbf{u}_t . Let a spatial embedding vector be

$$h_{i,t}^{(0)} = g_i(x_{i,t}) + \sum_{j=1}^3 \tilde{g}_j(u_{j,t})/3 \in \mathbb{R}^{d_1},$$

for $1 \leq i \leq p$. $\tilde{g}_j(u_{j,t})$ is a feature containing temporal information, and it plays a role in a dynamic and trainable positional encoding in transformer (Vaswani et al., 2017). Let $H_t^{(0)}$ be a $p \times d_1$ matrix, having $h_{i,t}^{(0)}$ as the i^{th} row vector, which is a collection of spatial embedding vectors across all sites. Then, SCAN is defined by (4), a self-attention for $H_t^{(0)}$ that is a map from $\mathbb{R}^{p \times d_1}$ to $\mathbb{R}^{p \times d_2}$ with a triplet of $d_1 \times d_2$ attention weight matrices $\mathbf{W}^{(0)} = (W_Q^{(0)}, W_K^{(0)}, W_V^{(0)})$.

$$H_t^{(1)} = \mathcal{Z}(H_t^{(0)}; \mathbf{W}^{(0)}, M_S) \in \mathbb{R}^{p \times d_2}. \quad (4)$$

$H_t^{(1)}$ is regarded as a spatial feature matrix corresponding to \mathbf{x}_t reweighted by causally constrained weights in Assumption 2.

4.3 Temporal Attention Network

The temporal attention network (TAN) is a specially designed self-attention to transform a series of B past spatial features obtained in (4). The TAN aligns with a similar concept of devising the transformer decoder (Vaswani et al., 2017) that satisfies predictability in forward feeding. However, the TAN distinguishes itself by employing a reduced input to compute an attention weight efficiently. The TAN incorporates (5) as an input value while employing (6) as the query and key. The dimensions of the query and key are reduced by a variable selection network (VSN) (Lim et al., 2021).

$$\mathbf{H}_t^{(1)} = [\text{vec}(H_{t-B+1}^{(1)})^\top, \dots, \text{vec}(H_t^{(1)})^\top]^\top \in \mathbb{R}^{B \times p d_2}, \quad (5)$$

where $\text{vec}(\cdot)$ denotes a flattening map, and

$$\tilde{\mathbf{H}}_t^{(1)} = [\text{VSN}_1(H_{t-B+1}^{(1)})^\top, \dots, \text{VSN}_1(H_t^{(1)})^\top]^\top \in \mathbb{R}^{B \times d_2}. \quad (6)$$

Each row of $\tilde{\mathbf{H}}_t^{(1)}$ is a reduced vector on \mathbb{R}^{d_2} corresponding to $H_{t'}^{(1)}$ for $t-B < t' \leq t$. The VSN layer performs compression by transforming a matrix of regional information into a single vector. Details of $\text{VSN}_1(\cdot)$ are

presented in the Appendix. The subscript of $\text{VSN}_1(\cdot)$ is used to distinguish it from other functions of the same form that will be used for different purposes later. Then, the TAN is defined by

$$\mathbf{H}_t^{(2)} = \text{TAN}(\tilde{\mathbf{H}}_t^{(1)}, \mathbf{H}_t^{(1)}; \mathbf{W}^{(1)}, M_T) := A^{(1)} \mathbf{H}_t^{(1)} \in \mathbb{R}^{B \times p d_2}$$

where $A^{(1)} = \text{softmax}(\tilde{\mathbf{H}}_t^{(1)} W_Q^{(1)} (\tilde{\mathbf{H}}_t^{(1)} W_K^{(1)})^\top / \sqrt{d_3} \odot M_T)$,

$\mathbf{W}^{(1)} = (W_Q^{(1)}, W_K^{(1)}) \in \mathbb{R}^{d_2 \times d_3} \times \mathbb{R}^{d_2 \times d_3}$, and M_T is the decoder mask. The upper diagonal elements in M_T are $-\infty$ such that $(A^{(1)})_{ij} = 0$ for $i < j$ and the i^{th} row of TAN only consists of the j^{th} row vector of $\mathbf{H}_t^{(1)}$ for $j \leq i$. Thus, the TAN preserves the irreversibility of the temporal features.

Note that all quantities defined in Section 4.3-4.5 depend on t because TAN aggregates past information across $t-B < t' \leq t$ at a current time point t . Unlike intermediate outputs in (4), the outputs of TAN for the same time point t' can differ depending on t . For example, the TAN output corresponding to time point $t-B+1$ in $\mathbf{H}_t^{(2)}$, i.e., the 1st row of $\mathbf{H}_t^{(2)}$ is distinct from one in $\mathbf{H}_{t-1}^{(2)}$ because $\mathbf{H}_{t-1}^{(2)}$ can exploit the information for time point $t-B$ while $\mathbf{H}_t^{(2)}$ can't. For notational simplicity, we omit the dependency with current t . For example, let $h_{t'}^{(2)} \in \mathbb{R}^{1 \times p d_2}$ be the $(t' - t + B)^{\text{th}}$ row vector of $\mathbf{H}_t^{(2)}$ corresponding to time $t-B < t' \leq t$.

4.4 Constrasting Spatial Dependence

The TAN uses the spatially collapsed features by the VSN such that spatial causality induced by Assumption 2 is blurred in $\mathbf{H}_t^{(2)}$. We add the contrasting step that constructs a spatially dependent feature. For $\mathbf{H}_t^{(2)}$, let $H_{t'}^{(2)} \in \mathbb{R}^{p \times d_2}$ be the reshaped matrix of $h_{t'}^{(2)}$, the $(t' - t + B)^{\text{th}}$ row vector of $\mathbf{H}_t^{(2)}$. The contrasted feature of $\mathbf{H}_t^{(2)}$ is given by

$$H_{t'}^{(3)} = \mathcal{Z}(H_{t'}^{(2)}; \mathbf{W}^{(2)}, M_S). \quad (8)$$

(8) is also the SCAN defined in (4), and it integrates temporal information with spatial information, resulting in more enriched representation learning. The attention weights of (8) are used to interpret and quantify spatial effects.

After the SCAN contrasting $\mathbf{H}_t^{(2)}$, the final output of the InstaTran's encoder is established by $\mathbf{H}_t^{(3)}$. We feed $H_{t'}^{(3)}$ to $\text{VSN}_2(\cdot)$ that transfers summarized information to the decoder. Similarly in (6), let $\mathbf{H}_t^{(3)}$ be the concatenated matrix with the context vectors of $H_{t'}^{(3)}$ for $t-B < t' \leq t$, where

$$\mathbf{H}_t^{(3)} = [\text{VSN}_2(H_{t-B+1}^{(3)})^\top, \dots, \text{VSN}_2(H_t^{(3)})^\top]^\top \in \mathbb{R}^{B \times d_2}. \quad (9)$$

The importance of the variable to return $\hat{\mathbf{y}}_{t,Q}^\tau$, is evaluated by the variable selection weights of the $\text{VSN}_2(\cdot)$. The details are discussed in Section 5.3. Thus far, we have explained the process in the spatiotemporal encoder.

4.5 Temporal Decoder

Inspired by the results of Wen et al. (2017), we propose a novel decoder architecture using the global and local context vectors from the feedforward network (FFN) layer. Our method incorporates two VSN layers in the decoder: the global VSN and the local VSN. The global VSN summarizes $\mathbf{H}_t^{(3)}$ and constructs a global context vector,

$$h_t^{(4)} = \text{VSN}_3(\mathbf{H}_t^{(3)}) \in \mathbb{R}^{d_2}. \quad (10)$$

The local VSN creates the local context vector by the embedded temporal feature encapsulating a locality in (11).

$$\tilde{v}_{t+k} = \text{VSN}_4([\tilde{g}_1(u_{1,t+k})^\top, \tilde{g}_2(u_{2,t+k})^\top, \tilde{g}_3(u_{3,t+k})^\top]^\top W^{(3)} + b^{(3)}) \in \mathbb{R}^{d_2} \quad (11)$$

where $W^{(3)} \in \mathbb{R}^{d_1 \times d_2}$ and $b^{(3)} \in \mathbb{R}^{d_2}$ denote trainable weight and bias vector, respectively. The two VSNs define a pooled context vector after time t by

$$\mathbf{V}_t = [v_{t+1}^\top, \dots, v_{t+\tau}^\top]^\top \in \mathbb{R}^{\tau \times d_2},$$

where $v_{t+k} = h_t^{(4)} + \tilde{v}_{t+k}$ for $k = 1, \dots, \tau$.

Next, the output of the encoder and the pooled context vector are concatenated as $\mathbf{H}_t^{(4)}$, which aggregates forward and backward available features at time t .

$$\mathbf{H}_t^{(4)} = [\mathbf{H}_t^{(3)\top}, \mathbf{V}_t^\top]^\top \in \mathbb{R}^{(B+\tau) \times d_2}. \quad (12)$$

To enrich the temporal feature, we convert $\mathbf{H}_t^{(4)}$ through the self-attention network in (13).

$$\mathbf{H}_t^{(5)} = \mathcal{Z}(\mathbf{H}_t^{(4)}; \mathbf{W}^{(4)}, M_T) \in \mathbb{R}^{(B+\tau) \times d_3}, \quad (13)$$

where $\mathbf{W}^{(4)} = (W_Q^{(4)}, W_K^{(4)}, W_V^{(4)})$.

$\mathbf{H}_t^{(5)}$ is the final feature of the decoder layer of the InstaTran. Our model can evaluate temporal importance via attention weights through the last self-attention layer (13). Using attention weights, we figure out the past time point that our model pays attention to and give a diagnosis on how it is consistent. The quantile output layer, which is the FFN layer, returns the k -step-ahead prediction at quantile level q , $\hat{\mathbf{y}}_{t,q}^\tau(k) \in \mathbb{R}$, $k = 1, \dots, \tau$ as follows:

$$\hat{y}_{t,q}^\tau(k) = (\mathbf{H}_t^{(5)})_{B+k,:} W_q^{(5)} + b_q^{(5)}, \quad q \in \mathcal{Q}, \quad (14)$$

where $W_q^{(5)} \in \mathbb{R}^{d_3 \times 1}$, $b_q^{(5)} \in \mathbb{R}^1$ are trainable parameters, and $(\mathbf{H}_t^{(5)})_{B+k,:}$ denotes the $(B+k)$ th row of $\mathbf{H}_t^{(5)}$, $k = 1, \dots, \tau$.

Note that our decoder predicts $\hat{y}_{t,q}^\tau$ directly, not recursively, and thus the model architecture is simple and efficient compared to the TFT. The decoders designed for direct forecasting (Chevillon, 2006; Taieb & Atiya, 2016; Wen et al., 2017) can improve performance by avoiding error accumulation causing biased forecasting. In practice, the proposed decoder is more potent than the one in the TFT in real data analysis (see Section 5.1).

4.6 Loss functions

We introduce the composite quantile loss (CQL) to forecast multiple quantiles. First, the quantile loss (QL) is defined by

$$\text{QL}(y, \hat{y}; q) = (q - \mathbb{I}_{\{y < \hat{y}\}}(y))(y - \hat{y}), \quad (15)$$

where $\mathbb{I}_{\mathcal{A}}(a)$ returns 1 for $a \in \mathcal{A}$ and 0, otherwise.

The InstaTran is trained by minimizing the CQL, which is defined as follows:

$$\text{CQL}(\mathbb{W}; \mathcal{T}, \mathcal{Q}, \tau) = \sum_{t \in \mathcal{T}} \sum_{q \in \mathcal{Q}} \sum_{k=1}^{\tau} \text{QL}(y_{t+k}, \hat{y}_{t,q}^\tau(k); q),$$

where \mathbb{W} denotes the entire weight and bias parameters and \mathcal{T} is the set of time points in the training dataset.

5 Experiments

We validate the effectiveness of the proposed model by evaluating the probabilistic forecasting and interpretability on a real-world dataset, the Han River water level dataset. As benchmark models we consider MQ-RNN(Wen et al., 2017), DeepAR(Salinas et al., 2020), and TFT (Lim et al., 2021). Among these benchmarks, the TFT exhibits the highest complexity, with a total of 99,497 parameters. The parameter counts for the remaining models are as follows: InstaTran - 77,047, DeepAR - 45,614, and MQ-RNN - 4,099, listed in ascending order.

The dataset is split into two segments: the training dataset from 2016 to 2020 and the test dataset in 2021. The hyperparameters of all models are selected by using a time series cross-validation. Each benchmark model predicts 12 hours' $\text{WL}(B_2)$ using the past 48 hours' data, i.e., $\tau = 12$ and $B = 48$. The target quantile is set by $\mathcal{Q} = \{0.1, 0.3, 0.5, 0.7, 0.9\}$. For both TFT and InstaTran, we summarize the importance of features by weights of the VSN layers. The experiments

are implemented with PyTorch on NVIDIA GeForce RTX 3090, and the source code is publicly available at <https://github.com/chulhongsung/InstaTran>.

For evaluation, we assess the performance of benchmark models using quantile loss (15) and calibration metric q -Rate (Chen et al., 2012; Wen et al., 2017).

$$q\text{-level QL} = \sum_{t \in \mathcal{T}'} \sum_{k=1}^{\tau} \text{QL}(y_{t+k}, \hat{y}_{t,q}^{\tau}(k); q) \quad (16)$$

$$q\text{-Rate} = \sum_{t \in \mathcal{T}'} \sum_{k=1}^{\tau} \frac{\mathbb{I}_{\{y_{t+k} < \hat{y}_{t,q}^{\tau}(k)\}}(y_{t+k})}{|\mathcal{T}'| \tau}, \quad (17)$$

where \mathcal{T}' denotes the set of time points in the test dataset.

The q -Rate is defined as the proportion of predictions below the q -level target, and it is desirable for the q -Rate to be close to the q -level. We conduct evaluations with different q levels at 0.5, 0.7, and 0.9.

5.1 Ablation studies of the InstaTran

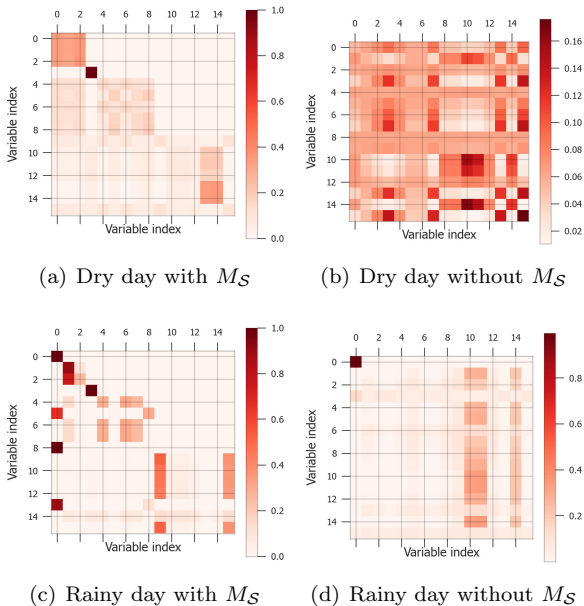


Figure 4: Attention weights of (8). (a) and (b) are cases on a dry day. (c) and (d) are cases on a rainy day. The x-axis and y-axis consist of variable indices: $\{0 : P_1, 1 : P_2, 2 : P_3, 3 : \text{WL}(B_5), 4 : \text{WL}(D), 5 : \text{IF}(D), 6 : \text{STR}(D), 7 : \text{JUS}(D), 8 : \text{OF}(D), 9 : \text{WL}(B_1), 10 : \text{FL}(B_1), 11 : \text{WL}(B_2), 12 : \text{WL}(B_3), 13 : \text{FL}(B_3), 14 : \text{WL}(B_4), 15 : \text{FL}(B_4)\}$.

Prior to comparing the benchmark models, we conduct ablation studies to show the merits of the spa-

tiotemporal encoders, SCAN and TAN in the InstaTran. First, we visualize the attention weights with and without the inclusion of M_S in (8), taking into account two scenarios: rainy and dry days. Figure 4 demonstrates the effectiveness of our spatially causal representation learning via the M_S . The colors of the i th row denote the importance of variables consisting of the i th feature. For example, the 3rd row in Figure 4 (c) exhibits dark colors in the 2nd and 3rd columns, which means that the 3rd row (feature) of $H_{t'}^{(3)}$ consists of the 2nd and the 3rd rows (features) of $H_{t'}^{(2)}$.

The results obtained with the mask exhibit reasonable outcomes, as they clearly distinguish between the two days and effectively capture the impact of rainfall on the dam and river during rainy conditions, aligning with our expectations. Conversely, in the cases where M_S is not applied, the attention weight does not provide a meaningful interpretation associated with the assumed spatial causality in Table 1.

Next, we evaluate the predictive capabilities of the proposed spatiotemporal encoder and the decoder. We consider four scenarios for the examination. The first involves the parallel attention that the SCAN and TAN separately feed their hidden features and learn spatial and temporal features independently; the second involves investigating the SCAN method without utilizing M_S ; the third focuses on the InstaTran model incorporating the TFT decoder; and the fourth explores the InstaTran model without any ablations. Table 2 illustrates the superior prediction performance of the proposed architecture. Compared to alternative models, the InstaTran model, incorporating our proposed structures, exhibits enhanced prediction accuracy across various quantile levels. Notably, it demonstrates superior calibration at a high quantile level of 0.9.

5.2 Comparison with other probabilistic forecasters

We evaluate the benchmark models with two metrics (16) and (17). Figure 5 shows examples of prediction results in the test set. The gray and black lines denote the past observations and target of the water level of B_2 , respectively. The lower and upper boundary of the blue band present predicted 0.1 and 0.9 level quantiles of the target. It is evident that the intervals generated by DeepAR are excessively wide, lacking sharpness, thereby rendering the results potentially meaningless. The MQ-RNN yields a biased interval to target levels. Conversely, the InstaTran and the TFT give reliable intervals at the sharp peak of the target (see total prediction results in Appendix).

Table 2: Performance metrics of variants of the InstaTran. The best results are marked in bold.

Metric	q	Parallel Attention	Without M_S	With TFT decoder	InstaTran
average q -level QL	0.9	0.0034	0.0025	0.0031	0.0021
	0.7	0.0072	0.0045	0.0051	0.0036
	0.5	0.0086	0.0048	0.0059	0.0040
q -Rate($ q - q\text{-Rate} $)	0.9	0.936(0.036)	0.946(0.046)	0.798(0.102)	0.924(0.024)
	0.7	0.894 (0.194)	0.838(0.138)	0.638(0.062)	0.796(0.096)
	0.5	0.823(0.323)	0.666(0.166)	0.623(0.123)	0.647(0.147)

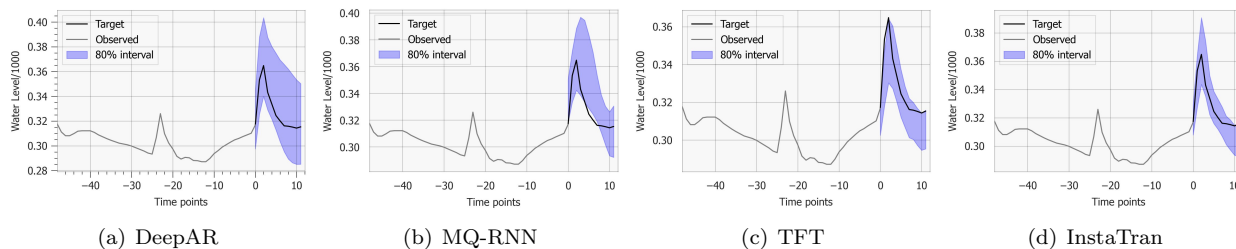


Figure 5: Example of prediction results in the test set.

Table 3: Performance metrics of benchmarks. The best results are marked in bold.

Metric	q	DeepAR	MQ-RNN	TFT	InstaTran
average q -level QL	0.9	0.0027	0.0030	0.0019	0.0021
	0.7	0.0044	0.0051	0.0031	0.0036
	0.5	0.0039	0.0053	0.0033	0.0040
q -Rate($ q - q\text{-Rate} $)	0.9	0.970(0.070)	0.930(0.030)	0.870(0.030)	0.924(0.024)
	0.7	0.925 (0.225)	0.788(0.088)	0.708(0.008)	0.796(0.096)
	0.5	0.788(0.288)	0.625(0.125)	0.392(0.108)	0.647(0.147)

Table 3 presents the performance results in the test dataset and shows that the TFT outperforms other models except for q -Rate at level 0.9. The InstaTran is competitive with the TFT in q -level QL; in particular, the InstaTran outperforms the others in q -Rate at level 0.9. Although DeepAR has a relatively lower quantile loss, Figure 5 and the q -Rate value in Table 3 emphasize its failure in accurate quantile predictions. See the total evaluation outcomes from May to October in Appendix for a comprehensive assessment.

5.3 Attribution Analysis

The importance of variables in the TFT and the InstaTran is computed at each time t through the VSN layer. The variable importance of the InstaTran is quantified through the weights of the VSN layer in (9), while for the TFT, it is measured by the weights of the 1st VSN layer. The weights of VSN can be interpreted as the variable’s attribution to the prediction because they are positive, and their summation is always 1.

Table 4 presents the mean, standard deviation, and

quantiles of each variable’s weight in the VSN layers. The InstaTran evaluates the importance of precipitations (v_1) more significantly than the TFT. The 0.9-quantile values of the precipitation importance do not exceed 0.06 for the TFT, whereas for the InstaTran, it is observed to have a much higher value of 0.25, indicating a relatively higher evaluation of precipitation importance in relation to water level variations.

The TFT gives the highest importance evaluation, with an average of 0.249, to the water level of B_2 . In our spatial causal assumption, the variability of B_2 can be explained by v_1, v_2 , and v_3 . The TFT model, which does not reflect this causal assumption, appears to evaluate the water level variations of the B_2 bridge primarily as a factor of v_4 . Thus, this phenomenon seems to be a result of the assumption of spatial causality not being incorporated into the TFT model. On the other hand, in the InstaTran which considers spatial causality, it is attainable to reflect the importance of v_1, v_2 , and v_3 , which can be understood through v_4 , through the VSN layer.

Figures 6(a) and 6(b) illustrate the observed values

Table 4: Descriptive statistics of variable importance. The most significant variables are marked in bold.

Node	Variable	TFT				InstaTran			
		Mean(Std)	0.1	0.5	0.9	Mean(Std)	0.1	0.5	0.9
v_1	P_1	0.031(0.007)	0.023	0.031	0.042	0.092(0.099)	0.006	0.062	0.249
	P_2	0.021(0.014)	0.008	0.017	0.030	0.042(0.030)	0.010	0.038	0.079
	P_3	0.034(0.015)	0.019	0.031	0.053	0.061(0.028)	0.034	0.053	0.104
v_2	WL(B_5)	0.131(0.016)	0.110	0.132	0.153	0.179(0.070)	0.058	0.201	0.251
	WL(D)	0.018(0.015)	0.006	0.013	0.040	0.088(0.075)	0.009	0.063	0.198
v_3	IF(D)	0.074(0.021)	0.005	0.070	0.101	0.074(0.038)	0.034	0.066	0.124
	STR(D)	0.018(0.007)	0.010	0.017	0.027	0.006(0.005)	0.003	0.005	0.011
	JUS(D)	0.012(0.011)	0.003	0.008	0.027	0.057(0.023)	0.034	0.053	0.083
	OF(D)	0.096(0.013)	0.080	0.095	0.111	0.048(0.025)	0.023	0.040	0.088
	WL(B_1)	0.040(0.014)	0.025	0.037	0.059	0.091(0.023)	0.055	0.097	0.114
v_4	FL(B_1)	0.015(0.007)	0.008	0.013	0.023	0.022(0.015)	0.008	0.017	0.046
	WL(B_2)	0.249(0.077)	0.148	0.253	0.348	0.084(0.048)	0.045	0.064	0.160
	WL(B_3)	0.019(0.004)	0.015	0.019	0.025	0.054(0.046)	0.008	0.038	0.117
	FL(B_3)	0.019(0.012)	0.009	0.016	0.034	0.040(0.081)	0.006	0.014	0.083
	WL(B_4)	0.082(0.024)	0.058	0.077	0.114	0.043(0.046)	0.011	0.020	0.114
	FL(B_4)	0.016(0.010)	0.007	0.014	0.028	0.014(0.040)	0.050	0.004	0.026

of precipitation P_1 , flow discharge OF, and their importance obtained from the VSN. In Figures 6(a) at $t = 20$, it is observed that there was heavy rainfall, while in Figure 6(b) at the same time point, a sharp increase in flow discharge is observed. Based on our assumptions, this indicates that the increase in discharge was due to heavy rainfall, resulting in an increase in the water level of the Han River. The dashed line in Figure 6(a) indicates that the InstaTran evaluates the importance of P_1 at a higher level after $t = 20$ for a certain period. In contrast, the TFT did not show any significant changes in the importance of P_1 during that period.

In Figure 6(a), it is observed that there was a marked rainfall at $t = 100$. Figure 6(b) indicates that the discharge was delayed after $t = 120$. In this case, the InstaTran did not assign higher importance to P_1 after $t = 100$. Instead, the InstaTran shows a higher evaluation of the importance of D . These two results conclude that the InstaTran evaluates a variable’s importance by considering both spatial and temporal structures, and it demonstrates a sustained effect over a specific period for extreme rainfall events. However, the InstaTran provides no apparent causality between rainfall events and delayed discharge.

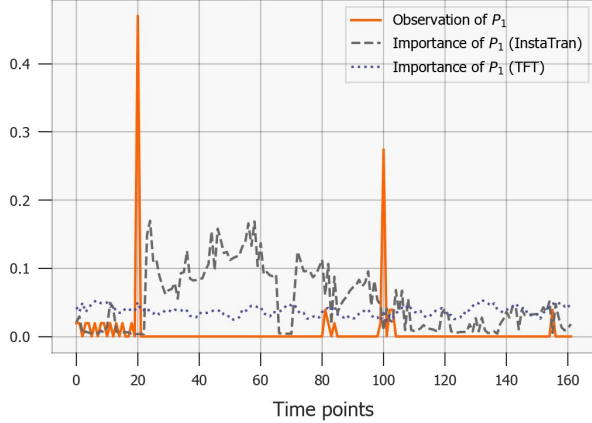
The standard deviations presented in Table 4 represent the variability of the VSN layer’s weight values at each time point, and larger standard deviations imply that the importance of variables varies over time. The InstaTran identifies variables with greater variability, indicating that these variables exhibit significant changes in their influence on the water level fluctuations of the Han River over time. Additionally,

there is a tendency for the mean to exceed the median in the InstaTran. It suggests a right-tailed distribution with substantial importance attributed to critical events such as extreme rainfall.

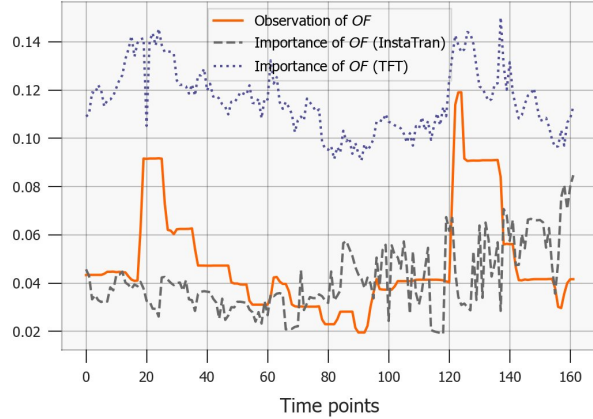
5.4 Consistent Temporal Patterns

The InstaTran’s encoder produces the output of the self-attention output, $H_t^{(5)}$ in (13) which consists of past time series variables and future time point variables. The attention weight of (13) represents the strength of association between predictor variables at past time points and future prediction time points at a time point t as the reference. Let the submatrix of the attention weight corresponding to the last τ rows and the 1st B columns be $A_t^{(5)}$. The element $(A_t^{(5)})_{kj}$ represents the weight indicating how much the feature at past time point $(t - B + j)$ influences the prediction at future time point $(t + k)$. Therefore, by examining $(A_t^{(5)})_{kj}$ for $j = 1, \dots, B$, we can show the magnitude of the influence of past feature variables on future predictions within the past B periods. Thus, we visualize the α -percentile of $(A_t^{(5)})_{kj}$ for $t \in \mathcal{T}, t > B$ obtained over the entire period as $w_\alpha^k(j)$ and illustrate them in Figure 7.

In Figure 7 (a), $w_{50}^1(j)$ demonstrates that the influence of past feature variables on predicting one time step ahead exhibits a periodic pattern over time. $w_{50}^2(j)$ illustrates the influence of past feature variables when predicting two-time steps ahead, showing a similar periodic pattern as $w_{50}^1(j - 1)$. This similarity generally holds for $w_{50}^{k+l}(j)$ and $w_{50}^k(j - l)$. It suggests that the attention weights between future predictions and past



(a) Importance of P_1 .



(b) Importance of $OF(D)$.

Figure 6: Variable importances and observations of P_1 and $OF(D)$. The solid line denotes the observations of variables. The dashed and dotted lines denote the importances of variables in the InstaTran and the TFT, respectively.

feature variables exhibit consistent functional patterns across time differences. Additionally, Figures 7 (c) and (d) display periodic functions with a period of 12 hours. It is conjectured that the periodic pattern is attributed to the characteristics of the tidal river.

6 Conclusion and Limitation

We propose a neural network model for multiple quantile prediction with spatiotemporal causal structure. Our model extends the existing transformer by alternating spatial and temporal masks, thereby incorporating prior knowledge into the feature learning of the model. Within the proposed model, spatial causality and temporal causality can be easily confirmed through the weights of the attention layers, and the importance of each variable can be identified through the VSN layer included in the model. The decoder of the proposed model has the advantage of using an attention model to output multiple quantiles for multiple time points simultaneously.

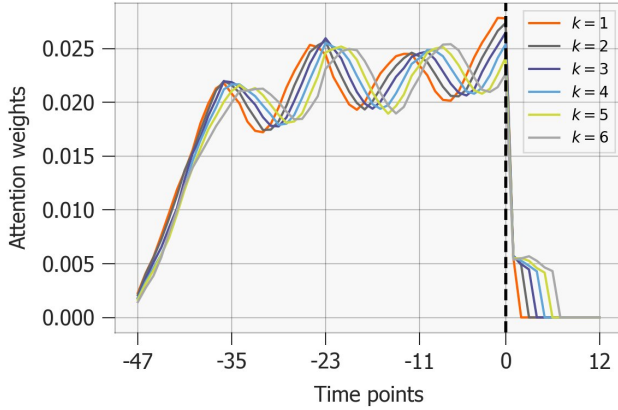
To validate the effectiveness of the proposed attention-building block, we conducted an ablation study using water level data from the Han River. First, the learned features in the model were found to satisfy the assumed spatiotemporal causality, and it was also observed that the importance of variables varied depending on specific events. From the ablation study, we confirmed that the constraints on spatiotemporal causal structure actually contribute to improving quantile prediction performance. Moreover, by examining the temporal attention weights of the proposed model, we can identify specific periodicities. This indicates

that the temporal attention of the proposed model identifies specific effects that can be captured through temporal differences and accurately represents their magnitudes as measures of importance. The learned variable importance and results related to temporal patterns within the model can be compared with existing prior knowledge, allowing us to determine whether the model satisfies the assumed physical constraints and whether new previously unknown patterns exist.

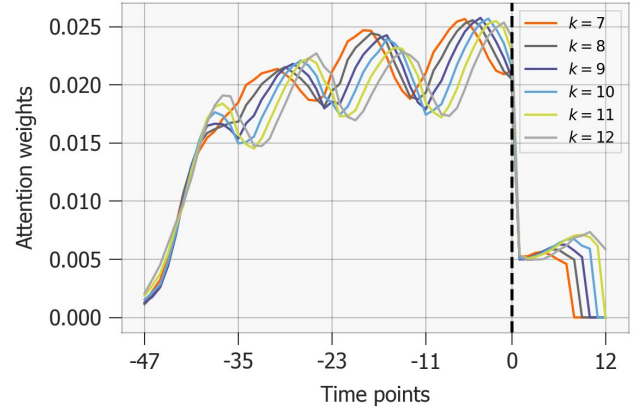
The proposed model significantly enhances the applicability of deep learning models by providing interpretable and diverse information that satisfies spatiotemporal causality. However, the constraint on a causal structure using attention masks does not constitute a complete causal model, such as structural causal models. The proposed model only maintains a simple causality structure, consisting of variable selection for constructing feature vectors and irreversibility related to temporal dependencies. Therefore, it does not inherently embed the causal structure in the latent space of the model in a general sense. It is expected that research in the nonlinear structural causal model would enable the construction of a more comprehensive interpretable deep-learning model. This aspect of the research is left for future investigations.

References

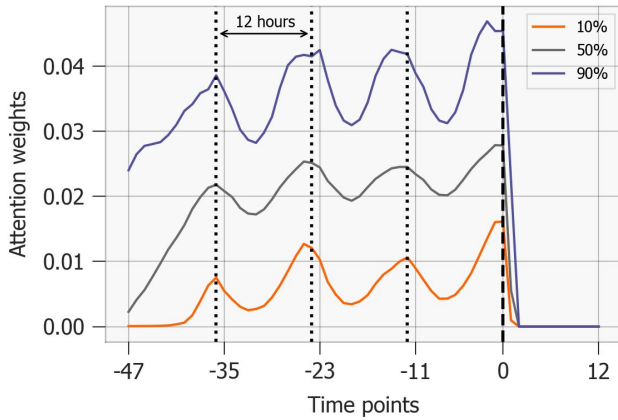
Aguilera, H., Guardiola-Albert, C., Naranjo-Fernández, N., and Kohfahl, C. Towards flexible groundwater-level prediction for adaptive water management: using facebook’s prophet forecasting



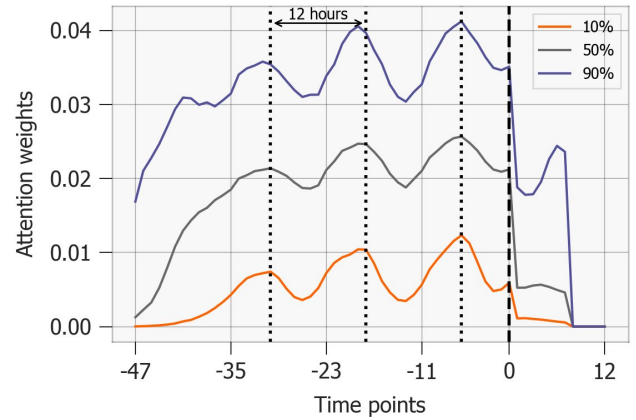
(a) $w_{50}^k(j), k \in \{1, \dots, 6\}$



(b) $w_{50}^k(j), k \in \{7, \dots, 12\}$



(c) $w_{\alpha}^1(j), \alpha \in \{10, 50, 90\}$



(d) $w_{\alpha}^6(j), \alpha \in \{10, 50, 90\}$

Figure 7: Attention weights of the last attention layer (13) for temporal patterns in the test set. Figure (a) and (b) presents the median (50th percentiles) of attention weights at various k . Figure (c) and (d) shows the percentiles of attention weights at 3 levels (10th, 50th, 90th) at $k = 1, 6$.

approach. *Hydrological Sciences Journal*, 64:1504 – 1518, 2019.

Avati, A., Jung, K., Harman, S., Downing, L., Ng, A., and Shah, N. H. Improving palliative care with deep learning. *BMC Medical Informatics and Decision Making*, 18, 2017.

Begoli, E., Bhattacharya, T., and Kusnezov, D. The need for uncertainty quantification in machine-assisted medical decision making. *Nature Machine Intelligence*, 1:20–23, 2019.

Benidis, K., Rangapuram, S. S., Flunkert, V., Wang, B., Maddix, D. C., Türkmen, A. C., Gasthaus, J., Bohlke-Schneider, M., Salinas, D., Stella, L., Calot, L., and Januschowski, T. Neural forecast-

ing: Introduction and literature overview. *ArXiv*, abs/2004.10240, 2020.

Carion, N., Massa, F., Synnaeve, G., Usunier, N., Kirillov, A., and Zagoruyko, S. End-to-end object detection with transformers. In *Computer Vision—ECCV 2020: 16th European Conference, Glasgow, UK, August 23–28, 2020, Proceedings, Part I 16*, pp. 213–229. Springer, 2020.

Castangia, M., Grajales, L. M. M., Aliberti, A., Rossi, C., Macii, A., Macii, E., and Patti, E. Transformer neural networks for interpretable flood forecasting. *Environmental Modelling & Software*, 160:105581, 2023.

Chatigny, P., Patenaude, J.-M., and Wang, S. Spatiotemporal adaptive neural network for long-term

- forecasting of financial time series. *International Journal of Approximate Reasoning*, 132:70–85, 2021.
- Chen, C. W., Gerlach, R., Hwang, B. B., and McAleer, M. Forecasting value-at-risk using nonlinear regression quantiles and the intra-day range. *International Journal of Forecasting*, 28(3):557–574, 2012.
- Chevillon, G. Direct multi-step estimation and forecasting. *Wiley-Blackwell: Journal of Economic Surveys*, 2006.
- Choi, Y., Cho, H., and Son, H. Capturing network and dynamic effects in bike sharing system via fused lasso. *arXiv preprint arXiv:2208.08150*, 2022.
- Civitarese, D. S., Szwarcman, D., Zadrozny, B., and Watson, C. Extreme precipitation seasonal forecast using a transformer neural network. *arXiv preprint arXiv:2107.06846*, 2021.
- Deng, L., Zhang, X., Tao, S., Zhao, Y., Wu, K., and Liu, J. A spatiotemporal graph convolution-based model for daily runoff prediction in a river network with non-euclidean topological structure. *Stochastic Environmental Research and Risk Assessment*, 2022.
- Ding, Y., Zhu, Y., Feng, J., Zhang, P., and Cheng, Z. Interpretable spatio-temporal attention lstm model for flood forecasting. *Neurocomputing*, 403:348–359, 2020.
- Hammoud, Z. and Kramer, F. Multilayer networks: aspects, implementations, and application in biomedicine. *Big Data Analytics*, 5(1):2, 2020.
- Huang, X., Chen, D., Ren, T., and Wang, D. A survey of community detection methods in multilayer networks. *Data Mining and Knowledge Discovery*, 35: 1–45, 2020.
- Jung, S., Cho, H., Kim, J., and Lee, G. Prediction of water level in a tidal river using a deep-learning based lstm model. *Journal of Korea Water Resources Association*, 51(12):1207–1216, 12 2018.
- Kaneko, Y. and Yada, K. A deep learning approach for the prediction of retail store sales. *2016 IEEE 16th International Conference on Data Mining Workshops (ICDMW)*, pp. 531–537, 2016.
- Kivelä, M., Arenas, A., Barthélemy, M., Gleeson, J. P., Moreno, Y., and Porter, M. A. Multilayer networks. *J. Complex Networks*, 2:203–271, 2013.
- Lim, B., Arık, S. Ö., Loeff, N., and Pfister, T. Temporal fusion transformers for interpretable multi-horizon time series forecasting. *International Journal of Forecasting*, 2021.
- Liu, Y., Hou, G., Huang, F., Qin, H., Wang, B., and Yi, L. Directed graph deep neural network for multi-step daily streamflow forecasting. *Journal of Hydrology*, 607:127515, 2022.
- Noor, F., Haq, S., Rakib, M., Ahmed, T., Jamal, Z., Siam, Z. S., Hasan, R. T., Adnan, M. S. G., Dewan, A., and Rahman, R. M. Water level forecasting using spatiotemporal attention-based long short-term memory network. *Water*, 2022.
- Park, C. G. and Baek, K. O. Reconsideration of evaluating design flood level at imjin river estuary. *Journal of Korea Water Resources Association*, 50(9): 617–625, 2017.
- Ruslan, F. A., Samad, A. M., Zain, Z. M., and Adnan, R. Flood water level modeling and prediction using narx neural network: Case study at kelang river. *2014 IEEE 10th International Colloquium on Signal Processing and its Applications*, pp. 204–207, 2014.
- Salinas, D., Flunkert, V., Gasthaus, J., and Januschowski, T. Deepar: Probabilistic forecasting with autoregressive recurrent networks. *International Journal of Forecasting*, 36(3):1181–1191, 2020.
- Sezer, O. B., Gudelek, M. U., and Ozbayoglu, A. M. Financial time series forecasting with deep learning: A systematic literature review: 2005–2019. *Applied soft computing*, 90:106181, 2020.
- Shen, W., Guo, Y., Wang, Y., Zhao, K., Wang, B., and Yuille, A. L. Deep regression forests for age estimation. In *Proceedings of the IEEE conference on computer vision and pattern recognition*, pp. 2304–2313, 2018.
- Shin, Y. K. and Yoon, K. S. The spatial distribution of water quality and sediments characteristics in the han river estuary. *Journal of the Geomorphological Association of Korea*, 12(4):13–23, 12 2005.
- Taieb, S. B. and Atiya, A. F. A bias and variance analysis for multistep-ahead time series forecasting. *IEEE Transactions on Neural Networks and Learning Systems*, 27:62–76, 2016.
- Vaswani, A., Shazeer, N. M., Parmar, N., Uszkoreit, J., Jones, L., Gomez, A. N., Kaiser, L., and Polosukhin, I. Attention is all you need. *ArXiv*, abs/1706.03762, 2017.
- Wen, R., Torkkola, K., Narayanaswamy, B., and Madeka, D. A multi-horizon quantile recurrent forecaster. *arXiv preprint arXiv:1711.11053*, 2017.

Wu, C., Zhang, X., Wang, W., Lu, C., Zhang, Y., Qin, W., Tick, G. R., Liu, B., and Shu, L. Groundwater level modeling framework by combining the wavelet transform with a long short-term memory data-driven model. *The Science of the total environment*, 783:146948, 2021.

Wu, Y., Ding, Y., Zhu, Y., Feng, J., and Wang, S. Complexity to forecast flood: Problem definition and spatiotemporal attention lstm solution. *Complexity*, 2020:1–13, 2020.

Yadav, B. and Eliza, K. A hybrid wavelet-support vector machine model for prediction of lake water level fluctuations using hydro-meteorological data. *Measurement*, 103:294–301, 2017.

Appendix

Descriptive statistics of variables.

Table 5 presents the basic statistics of variables. The observations of precipitations have most 0, but their maximum values are too big to have a high impact. There are some variables that have a larger standard deviation than the mean, such as $IF(D)$ and variables related to flow.

Table 5: Descriptive statistics of variables in the Han River dataset. *: The minimum value of $FL(B_3)$ can be negative due to barrages in the Han River or tide.

	Mean	Std	Min	25%	Median	75%	Max
P_1	0.03	0.24	0.0	0.0	0.0	0.0	8.5
P_2	0.04	0.27	0.0	0.0	0.0	0.0	9.33
P_3	0.03	0.24	0.0	0.0	0.0	0.0	8.0
$WL(B_5)$	346.49	171.89	55.33	194.83	324.50	485.33	811.33
$WL(D)$	25.04	0.14	24.13	24.94	25.04	25.14	25.42
$IF(D)$	590.45	1213.37	0.0	136.0	269.61	510.39	18830.0
$STR(D)$	212.71	5.32	178.37	209.36	212.92	216.46	226.46
$JUS(D)$	31.29	5.32	17.55	27.54	31.08	34.64	65.64
$OF(D)$	582.60	1213.05	0.0	134.0	216.17	503.0	18161.67
$WL(B_1)$	332.49	82.28	260.7	288.7	309.2	346.7	1287.2
$FL(B_1)$	784.05	1152.50	243.29	325.73	458.62	764.20	9405.6
$WL(B_2)$	319.79	72.96	250.37	279.87	300.2	334.37	1142.87
$WL(B_3)$	317.02	68.13	252.0	278.0	299.0	332.17	1067.67
$FL(B_3)$	640.25	1503.29	-3118.98*	215.05	373.21	720.21	24859.13
$WL(B_4)$	303.14	54.68	242.3	269.13	289.05	320.47	839.47
$FL(B_4)$	1130.82	1623.81	219.52	469.24	718.04	1219.26	29501.66

Variable Selection Network (VSN)

Lim et al. (2021) constructs the context vector by the VSN that averages over hidden states with trainable weights. Let $w(\phi_{t'}) \in \mathbb{R}^p$ be trainable weight vector of $\phi_{t'}$. Then, for $t - B < t' \leq t$, the output of the VSN layer is given by

$$\text{VSN}(\phi_{t'}) = \mathbf{1}_p \text{diag}(w(\phi_{t'})) \phi_{t'} \in \mathbb{R}^{d_2}, \quad (18)$$

where $\mathbf{1}_p$ is the row vector whose all elements are ones. For details on $w(\phi_{t'})$, see Section 4.2 of Lim et al. (2021). The weight vector $w(\phi_{t'})$ assumes a role in determining the significance of spatial variables learned from the initial SCAN layer, capable of capturing the significant event within a specific variable. Thus, the VSN reduces the spatial feature matrix $\phi_{t'}$ into the feature vector called a context vector. Let a collection of the context vectors from $t - B + 1$ to t be

$$\Phi_{t,B} = [\text{VSN}(\phi_{t-B+1})^\top, \dots, \text{VSN}(\phi_t)^\top]^\top \in \mathbb{R}^{B \times d_2}. \quad (19)$$

Total prediction results of benchmarks.

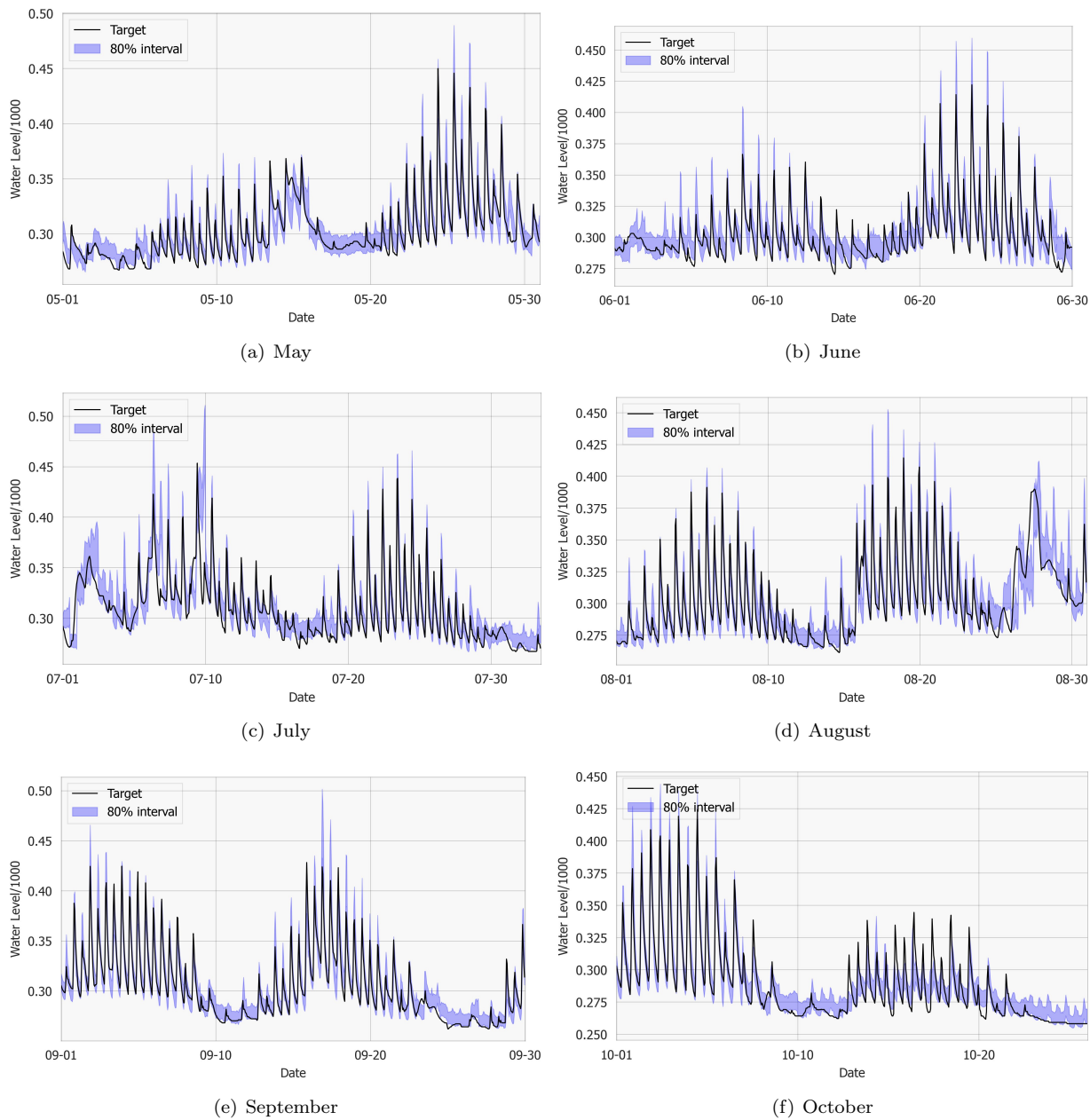
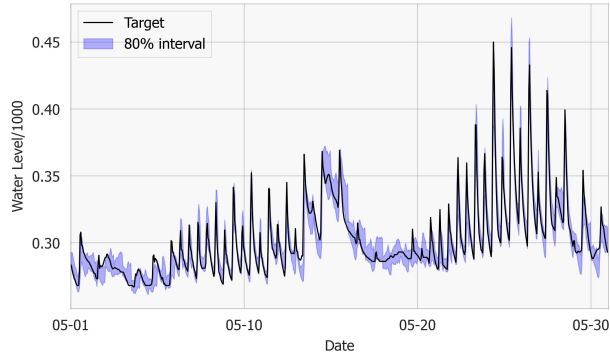
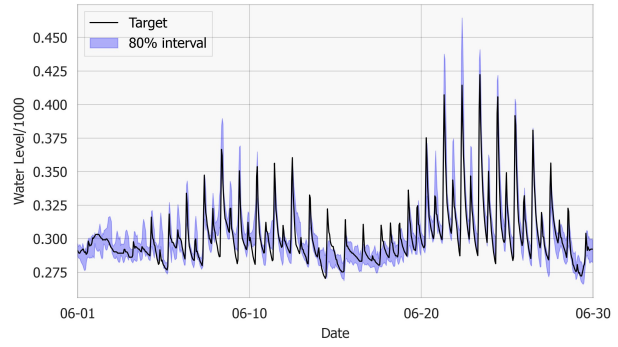


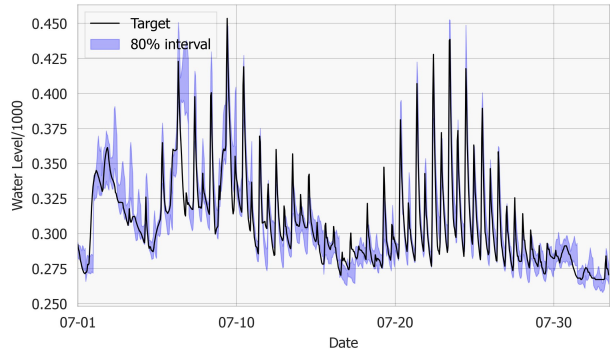
Figure 8: Total prediction results of the InstaTran.



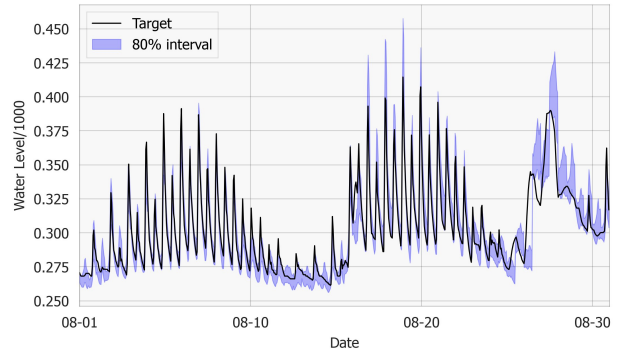
(a) May



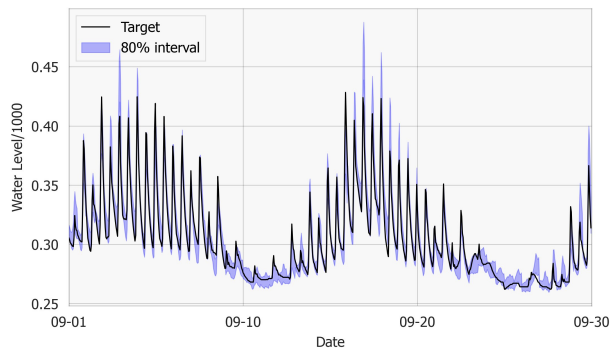
(b) June



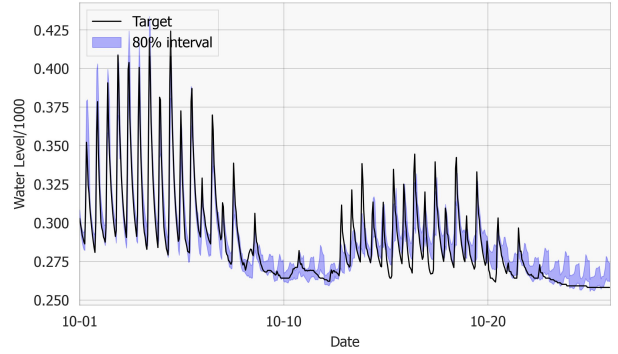
(c) July



(d) August

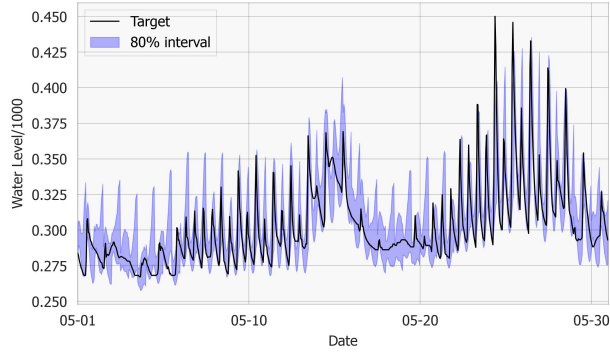


(e) September

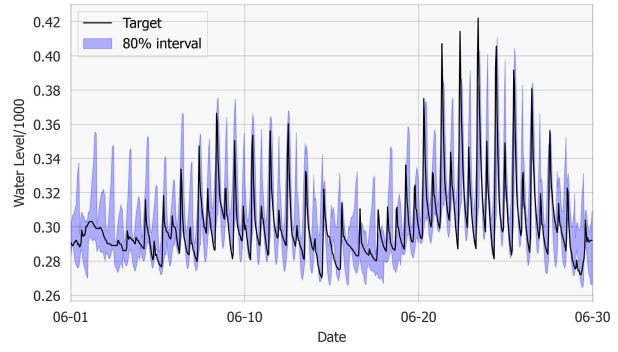


(f) October

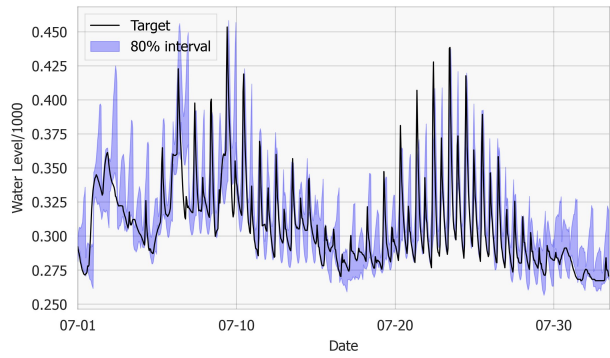
Figure 9: Total prediction results of the TFT.



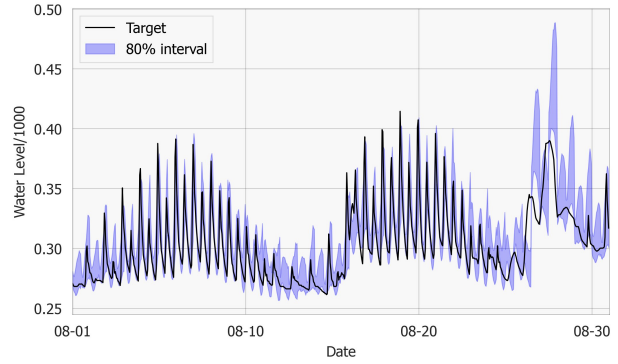
(a) May



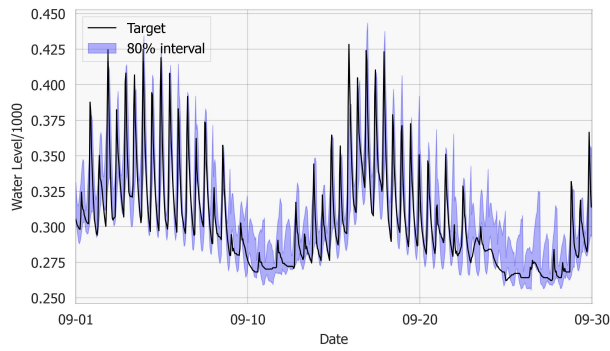
(b) June



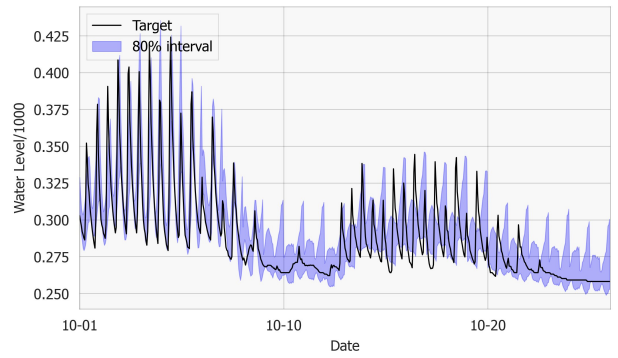
(c) July



(d) August

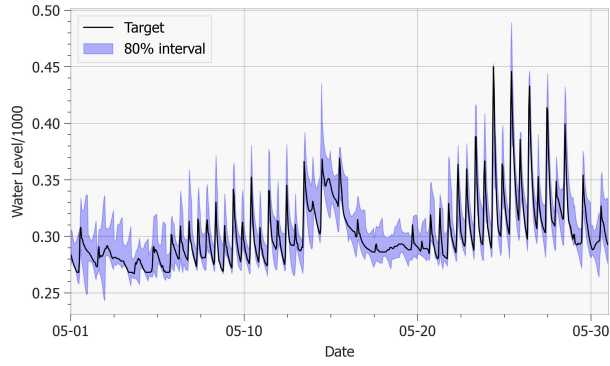


(e) September

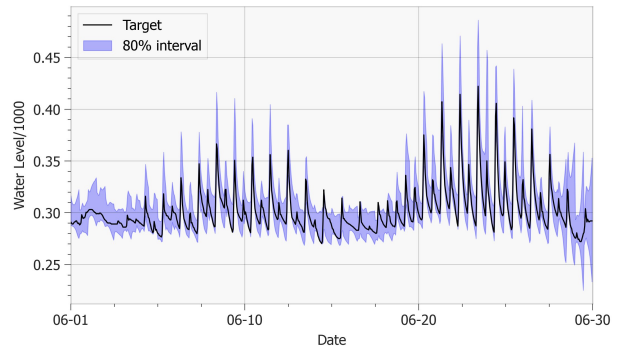


(f) October

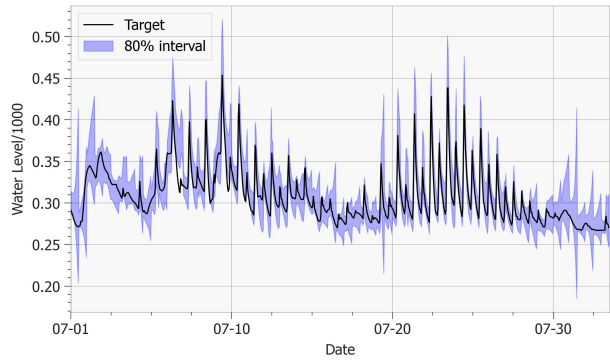
Figure 10: Total prediction results of the MQ-RNN.



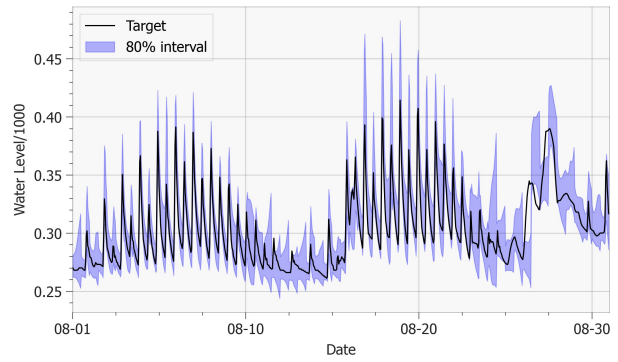
(a) May



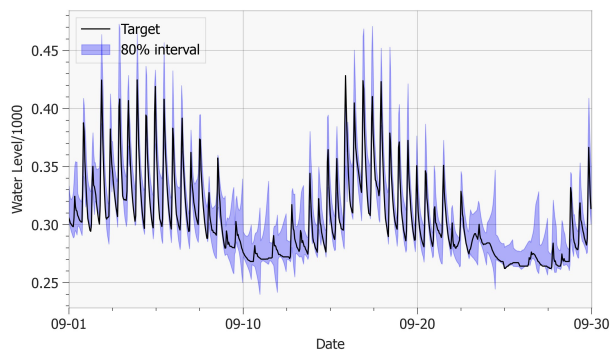
(b) June



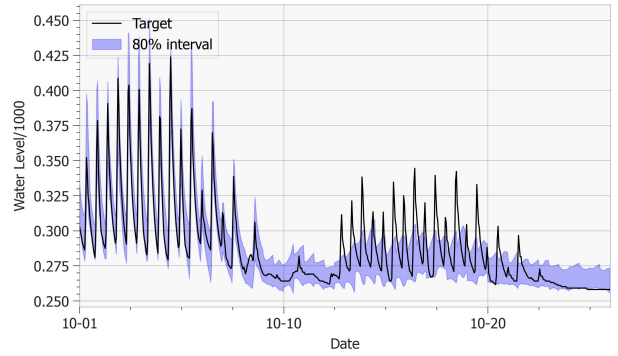
(c) July



(d) August



(e) September



(f) October

Figure 11: Total prediction results of the DeepAR.